Title

Fully Automated, Fast Motion Correction of Dynamic Whole-Body and Total-Body PET/CT Imaging Studies.

Journal

Journal of Nuclear Medicine, 64(7)

Authors

Shiyam Sundar, Lalith
Lassen, Martin
Gutschmayer, Sebastian
et al.

Publication Date

2023-07-01

DOI

10.2967/jnumed.122.265362

Fully Automated, Fast Motion Correction of Dynamic Whole-Body and Total-Body PET/CT Imaging Studies

Lalith Kumar Shiyam Sundar[1], Martin Lyngby Lassen[2], Sebastian Gutschmayer[1], Daria Ferrara[1], Anna Calabrò[3], Josef Yu[1], Kilian Kluge[4], Yiran Wang[3], Lorenzo Nardo[3], Philip Hasbak[2], Andreas Kjaer[2], Yasser G. Abdelhafez[3], Guobao Wang[3], Simon R. Cherry[3,5], Benjamin A. Spencer[3], Ramsey D. Badawi[3,5], Thomas Beyer[1], and Otto Muzik[6]

[1]Quantitative Imaging and Medical Physics Team, Center for Medical Physics and Biomedical Engineering, Medical University of Vienna, Vienna, Austria; [2]Department of Clinical Physiology, Nuclear Medicine, and PET and Cluster for Molecular Imaging Section 4011, Rigshospitalet, University of Copenhagen, Copenhagen, Denmark; [3]Department of Radiology, University of California–Davis, Davis, California; [4]Department of Biomedical Imaging and Image-Guided Therapy, Division of Nuclear Medicine, Medical University of Vienna, Vienna, Austria; [5]Department of Biomedical Engineering, University of California–Davis, Davis, California; and [6]Department of Pediatrics, Children's Hospital of Michigan, Wayne State University School of Medicine, Detroit, Michigan

We introduce the Fast Algorithm for Motion Correction (FALCON) software, which allows correction of both rigid and nonlinear motion artifacts in dynamic whole-body (WB) images, irrespective of the PET/CT system or the tracer. **Methods:** Motion was corrected using affine alignment followed by a diffeomorphic approach to account for nonrigid deformations. In both steps, images were registered using multiscale image alignment. Moreover, the frames suited to successful motion correction were automatically estimated by calculating the initial normalized cross-correlation metric between the reference frame and the other moving frames. To evaluate motion correction performance, WB dynamic image sequences from 3 different PET/CT systems (Biograph mCT, Biograph Vision 600, and uEXPLORER) using 6 different tracers (^{18}F-FDG, ^{18}F-fluciclovine, ^{68}Ga-PSMA, ^{68}Ga-DOTATATE, ^{11}C-Pittsburgh compound B, and ^{82}Rb) were considered. Motion correction accuracy was assessed using 4 different measures: change in volume mismatch between individual WB image volumes to assess gross body motion, change in displacement of a large organ (liver dome) within the torso due to respiration, change in intensity in small tumor nodules due to motion blur, and constancy of activity concentration levels. **Results:** Motion correction decreased gross body motion artifacts and reduced volume mismatch across dynamic frames by about 50%. Moreover, large-organ motion correction was assessed on the basis of correction of liver dome motion, which was removed entirely in about 70% of all cases. Motion correction also improved tumor intensity, resulting in an average increase in tumor SUVs by 15%. Large deformations seen in gated cardiac ^{82}Rb images were managed without leading to anomalous distortions or substantial intensity changes in the resulting images. Finally, the constancy of activity concentration levels was reasonably preserved (<2% change) in large organs before and after motion correction. **Conclusion:** FALCON allows fast and accurate correction of rigid and nonrigid WB motion artifacts while being insensitive to scanner hardware or tracer distribution, making it applicable to a wide range of PET imaging scenarios.

Key Words: whole-body PET; total-body PET; motion correction; diffeomorphic registration; automation; quantification

J Nucl Med 2023; 64:1145–1153
DOI: 10.2967/jnumed.122.265362

PET is a widely used medical imaging technique that enables noninvasive visualization of molecular processes in the body. New PET/CT systems with an extended axial field of view now allow for total-body (TB) PET imaging using a single bed position (*1*), offering improved volume sensitivity and the ability to acquire TB pharmacokinetic data with short frame durations (*2*). However, these advances require improved methods for motion correction to enable improved whole-body (WB) image analysis, such as parametric imaging. Currently, there is no motion correction software that works effectively for both WB (acquisition of multiple bed positions) or TB (one large axial FOV bed position) dynamic PET imaging or that is universal across all tracers and organs.

Rigid motion is typically encountered in brain studies, and many methods have been proposed to correct subject head motion effectively (*3–5*). Likewise, numerous nonrigid motion compensation approaches (*6–9*) have been proposed to selectively compensate for respiratory and cardiac motion in PET imaging studies. However, the literature is rather sparse (*10,11*) regarding TB/WB motion correction approaches that can universally and automatically compensate for both rigid and nonrigid motion.

WB/TB dynamic PET motion correction aims to achieve voxelwise correspondence in a series of image frames. Motion artifacts arise from involuntary movements, such as breathing and cardiac motion or voluntary changes in body position due to patient fatigue or pain. Motion correction for WB/TB PET imaging is a complex problem because of 2 main challenges: the time-dependent changes in tracer distribution and the variable rigidity profiles of different organs, some being rigid (e.g., brain) and others being deformable (e.g., heart). Therefore, it is challenging for a single alignment algorithm to account for both profiles robustly. Likewise, different tracers produce unique tracer distribution images because of varying kinetics. Therefore, a motion compensation paradigm that works on one tracer might not necessarily work on another.

To add complexity, different acquisition protocols can present different challenges for realignment. For example, in research, dynamic studies are often initiated contemporaneously with tracer injection, showing significant variation in tracer distribution. Consequently, motion correction is seldom performed during the first 10 min after injection. To date, there are no promising techniques to perform robust motion correction in the early frames (<10 min after injection). In clinical scenarios, studies with a small number of

---

Received Dec. 22, 2022; revision accepted Mar. 9, 2023.
For correspondence or reprints, contact Otto Muzik (otto@pet.wayne.edu).

image frames are acquired during the equilibrium phase (when tracer changes are negligible) to enable accurate correction of motion artifacts. Because clinical or research studies likely fall between these 2 extreme protocols, developing multiple alignment strategies tailored to one or the other acquisition protocol is impractical.

In response to these challenges, we focused on creating a generic, fully automated motion correction tool that gracefully adapts to these challenges. We present the Fast Algorithm for Motion Correction (FALCON) tool, a new WB/TB motion correction tool based on multiscale Greedy diffeomorphic registration paradigms (*12*). Diffeomorphism refers to a type of mathematic transformation that is smooth and invertible. This type of registration has been extensively used in computational neuroanatomy (*13–16*) because it can handle large, nonlinear deformations while preserving image topology. Since diffeomorphisms have shown great success in aligning highly deformable organs (*17*), we hypothesized that a diffeomorphic algorithm would be well suited to aligning different WB image frames of a subject across time. In addition to developing an accurate motion compensation scheme, we also focused on addressing the problem of rapidly changing uptake patterns during the initial part of the study ($<$10 min after injection), which renders accurate motion correction of early frames an ill-conditioned problem.

MATERIALS AND METHODS

Ethics Declaration

All data were acquired in accordance with the Declaration of Helsinki. Written informed consent was obtained from all subjects before the examinations. Approval numbers for the various datasets are presented in Table 1.

Identification of Frames Eligible for Motion Correction

In dynamic PET series, not all frames can be accurately aligned with the reference frame (typically the last frame). Early frames (those occurring within the first 10 min) differ notably from the reference frame. It would be advantageous to objectively select the frames for which alignment with the reference frame can be reliably performed. Therefore, a precomputational step was devised to enable automated identification of frames on which motion correction can robustly be performed (termed candidate frames), irrespective of the acquisition protocol (Fig. 1).

A voxelwise normalized cross-correlation (NCC) image was calculated between the 3-dimensional (3D) reference frame F and the moving frames $I_{i,j}$ (varying from time point i to j) by…

$$\mathrm{NCC}_{i,j} = \frac{\sum_{x,y,z}\left(I_{i,j}(x,y,z)-\mu_{i,j}\right)\left(F(x,y,z)-\mu_F\right)}{\sqrt{\sum_{x,y,z}\left(I_{i,j}(x,y,z)-\mu_{i,j}\right)^2}\sqrt{\sum_{x,y,z}\left(F(x,y,z)-\mu_F\right)^2}}, \qquad \text{(Eq. 1)}$$

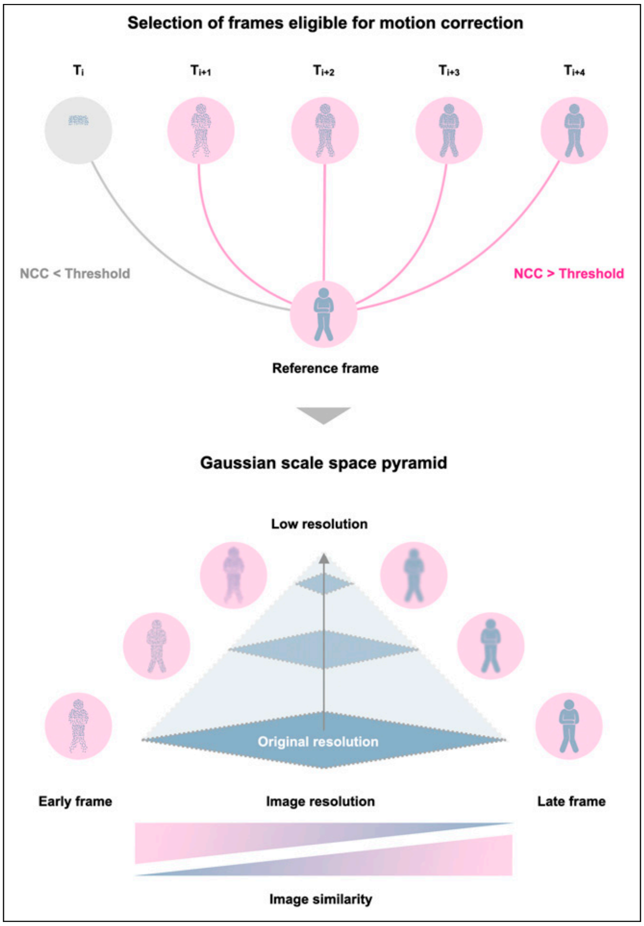

FIGURE 1. FALCON algorithm begins by selecting frames eligible for motion correction using customized threshold for NCC. These frames are then embedded in gaussian scale space pyramid and registered using multiscale registration. As resolution decreases, image similarity increases.

where $\mu_{i,j}$ and μ_F are the mean intensities of $I_{i,j}$ and F. After calculation of the voxelwise NCC image for each image pair, the corresponding mean NCC $\mu_{\mathrm{NCC}_{i,j}}$ was calculated for the so-derived NCC images:

$$\mu_{\mathrm{NCC}_{i,j}} = \frac{\sum_{x,y,z}\mathrm{NCC}_{i,j}(x,y,z)}{N}, \qquad \text{(Eq. 2)}$$

where N is the total number of voxels in the image. Finally, frames on which motion correction can effectively be performed

TABLE 1
Dataset Approvals

Dataset	Acquisition system	Institutional review board	Reference number
^{18}F-FDG (n = 8)	Biograph Vision 600	Medical University of Vienna	EK1907/2020
^{68}Ga-PSMA (n = 8)	Biograph Vision 600	Medical University of Vienna	EK1907/2020
^{11}C-PIB (n = 6)	Biograph Vision 600	Medical University of Vienna	EK1907/2020
^{18}F-FDG (n = 10)	uEXPLORER	University of California, Davis	IRB # 1374902
$^{68.}$Ga-DOTATATE (n = 8)	uEXPLORER	University of California, Davis	IRB # 1470016
^{18}F-fluciclovine (n = 8)	uEXPLORER	University of California, Davis	IRB # 1470016
^{82}Rb (n = 11)	Biograph mCT	Rigshospitalet Copenhagen	H-15009293

were identified using the following criteria:

$$I_{i,j} \mid \mu_{\mathrm{NCC}_{i,j}} > 0.6 \cdot \max_{i,j}\left(\mu_{\mathrm{NCC}_{i,j}}\right), \qquad \text{(Eq. 3)}$$

where $I_{i,j}$ represents the set of images with a corresponding mean NCC ($\mu_{\mathrm{NCC}_{i,j}}$) greater than 60% of the maximum mean NCC across all frames.

A threshold of 60% was chosen as the minimum acceptable level of similarity for an image to be considered a candidate frame in a dynamic series. The rationale behind this threshold is that an image with a mean NCC of more than half of the observed maximum mean NCC in a dynamic series is likely to have sufficient similarity to the reference image, making it a good candidate for motion correction.

Motion Correction Methodology and Scale Space

Motion correction was performed on only the candidate frames using 2 sequential steps. First, an affine alignment was used to correct for global motion, such as movement of the head and extremities. Second, a Greedy diffeomorphic approach was used to account for precise nonrigid motion such as lung deformation, intestine movement, and bladder distention. The diffeomorphic approach is "greedy," as the optimization is performed by making a locally optimal choice to find a global optimum subsequently (*18*). The paradigm uses a nonlinear optimization approach to align 2 images by iteratively deforming one image to the other by maximizing their similarity metric. In both steps, images are registered in gaussian scale space following a multiscale alignment approach (Fig. 1). Specifically, the algorithm conducts affine and diffeomorphic alignment between images starting at a coarse scale that is then used to initialize registration at the next finer scale, a process repeated until it reaches the finest possible scale. The multiscale methodology has several advantages that facilitate fast and robust alignment of images: first, the computational load is reduced significantly since most iterations are performed at the coarse levels of the pyramid. Second, the algorithm is less likely to get trapped in a local optimum because the initial search is performed on a coarse grid (*19*). In addition, using an approach with gaussian scale space improves the similarity between early and late frames in an image sequence by suppressing high-frequency information, such as noise in the early frames and structural information in the late frames (Fig. 1).

Unlike most registration algorithms, which apply a normalized-mutual-information metric, we chose the NCC as the similarity metric. Our choice was guided by the understanding that the normalized-mutual-information metric is poorly suited to deformable registration because of the many degrees of freedom, which lead to nonrealistic spatial deformations (*12,16*). In contrast, the NCC metric uses small-volume patches and is therefore much more constrained, thus resulting in more realistic alignments (*12*).

Mathematically, we can represent the images being registered as I_1 and I_2 and the deformation field as ϕ. The NCC between the images is then given by…

$$\mathrm{NCC}(I_1, I_2, \phi) = \frac{\sum_{x \in \Omega}\left(I_1(x) - \mu_{I_1}\right)\left(I_2(\phi(x)) - \mu_{I_2}\right)}{\sqrt{\sum_{x \in \Omega}\left(I_1(x) - \mu_{I_1}\right)^2}\sqrt{\sum_{x \in \Omega}\left(I_2(x) - \mu_{I_2}\right)^2}}, \qquad \text{(Eq. 4)}$$

where μ_{I_1} and μ_{I_2} are the means of the images I_1 and I_2, and omega is the domain over which the NCC is calculated. The Greedy diffeomorphic algorithm aims to find a deformation field ϕ that maximizes the NCC.

Software Implementation

The software is built around the Greedy Registration Toolkit (*12*) and Kitware's Insight Segmentation and Registration Toolkit (*20,21*). A comprehensive exposition on the image registration procedure and the corresponding hyperparameter specifications can be found in the supplemental materials (available at http://jnm.snmjournals.org). Images are aligned at 3 different resolution levels of a scale space pyramid: coarse (one-eighth resolution), medium (one-fourth resolution), and fine (original resolution) (*19*). Moreover, the user can select the number of maximum iterations for aligning the images at each resolution level, with 100, 50, and 25 (coarse, medium, and fine, respectively) iterations set as the default, which proved to be a solid choice on testing during development to compromise speed and robustness. The software runs the alignment in parallel by default, and the speed of the motion correction increases with the number of available central-processing-unit cores.

The code for FALCON is freely available under an open-source license. Interested users can access the code by visiting the FALCON GitHub page (https://github.com/QIMP-Team/FALCON). The code is regularly updated and maintained by the FALCON development team. Instructions for downloading and installing the software can be found on the GitHub page. Sample videos of before and after motion correction can be found on YouTube (http://bit.ly/3FXxDO0).

Performance Assessment

We applied the developed software to studies of patients with various cancer types who underwent dynamic imaging procedures using different tracers on 2 different PET/CT systems (Siemens Biograph Vision 600 and United Imaging uExplorer). Specifically, 3 separate studies were acquired using the Biograph Vision 600 (axial field of view, 26 cm). In the first study, 8 lung cancer patients (47–77 y old, 50–88 kg, 4 women and 4 men) underwent WB PET using ^{18}F-FDG as a tracer (injected dose, 309 ± 52 MBq). Likewise, 8 additional prostate cancer patients (51–77 y, 63–164 kg) underwent WB PET using ^{68}Ga-PSMA as a tracer (injected dose, 161 ± 22 MBq). The acquisition protocol for both studies was identical. After intravenous injection of the activity, a 6-min dynamic scan with the bed fixed at the chest region was followed by a 60-min dynamic WB PET scan consisting of 14 continuous-bed-motion passes. From the 66-min PET acquisition, only the continuous 6- to 66-min WB PET scan was considered for motion correction since it covered the entire body. The PET list-mode data were rebinned into a dynamic frame sequence (6 × 180 s and 8 × 330 s). In the third study, 6 patients with cardiac amyloidosis (48–82 y old, 58–91 kg, 2 women and 4 men) were scanned using ^{11}C-Pittsburgh compound B (PIB) (703 ± 51 MBq), and a 25-min list-mode acquisition with continuous-bed-motion passes was initiated from 10 min after injection. The list-mode data were subsequently rebinned into a 5 × 300 s dynamic sequence. Images of all studies were reconstructed into 220 × 220 matrices (voxel size, 3.3 × 3.3 × 2.0 mm) using 3D point-spread function plus time-of-flight ordered-subsets expectation maximization with all corrections applied.

In addition, 3 studies with different tracers were acquired using the uEXPLORER (axial field of view, 194 cm). In the first study, 10 patients with genitourinary cancer (56–82 y old, 64–101 kg, 9 men and 1 woman) underwent a 60-min PET list-mode acquisition after injection of ^{18}F-FDG (351 ± 17 MBq); the acquisition was subsequently rebinned into a dynamic frame sequence (6 × 10 s, 2 × 30 s, 6 × 60 s, 5 × 120 s, 4 × 180 s, and 6 × 300 s). In the second study, 8 patients with recurrent prostate cancer (66–90 y old, 71–109 kg) were scanned using ^{18}F-fluciclovine (310 ± 4 MBq), with the resulting list-mode data being rebinned into a 25-min dynamic frame sequence (12 × 5 s, 3 × 10 s, 3 × 30 s, 6 × 60 s, and 8 × 120 s). In the third study, 8 patients with neuroendocrine tumors (49–92 y old, 47–102 kg, 3 men and 5 women) underwent a 20-min list-mode acquisition using ^{68}Ga-DOTATATE (181 ± 18 MBq) starting at 60 min after injection, with the data rebinned into a dynamic frame sequence (20 × 60 s). All images acquired using the uEXPLORER were reconstructed into 150 × 150 matrices (voxel size, 4 × 4 × 4 mm) using 3D time-of-flight ordered-subsets expectation maximization with all corrections (except for point-spread-function modeling).

As a result, the performance of the motion correction algorithm was evaluated for 5 tracers (^{18}F-FDG, ^{68}Ga-PSMA, ^{11}C-PIB, ^{18}F-fluciclovine, and ^{68}Ga-DOTATATE) using 3 different measures. First, correction of overall gross body motion across the dynamic sequence was assessed on the basis of the volume mismatch between the individual WB image volumes. Specifically, a 3D body surface was determined semiautomatically using thresholding across the dynamic sequence, thereby defining a body volume for each frame. The so-derived body volumes were then subtracted in 3D space from the reference body volume (last) frame, yielding a mismatch volume (mm^3). Mismatch volumes were determined for both the motion-corrected and the uncorrected dynamic sequences. The percentage decrease in mismatch volume was then used to measure motion correction performance concerning gross body motion artifacts. In addition, the segmented body volumes were averaged across the frames for both the motion-corrected and the uncorrected dynamic sequences for all tracers. The resulting penumbra images, or the probabilistic binary masks, ranged from 0 to 1, where 0 indicates complete mismatch and 1 indicates complete overlay. This approach was especially useful in evaluating the motion correction performance for the head and extremities. The proposed approach is analogous to the calculation of a Dice coefficient. However, it is much more sensitive in highlighting mismatches.

Second, to evaluate the accuracy of the developed method to correct for involuntary motion within the torso due to respiration, the superior surface of the liver (termed the liver dome) was defined manually by a nuclear medicine expert in 3 coronal slices that were 2 cm apart in all motion-corrected and uncorrected images. The absolute difference between the so-defined liver dome of the reference frame (last) and all other dynamic frames was calculated and compared for both motion-corrected and uncorrected images for all tracers. Finally, the absolute average distance (mm) was reported.

Third, to evaluate the impact of the motion correction algorithm on lesion intensity in clinical oncologic scans, we manually defined a small ($<$10 cm^3) tumor tissue nodule on the average image of the dynamic series of each patient and calculated the associated SUV$_{\text{mean}}$. Only small tumors ($<$10 cm^3) were selected because they were more prone to motion artifacts. The tumors were segmented by a nuclear medicine physician using a semiautomated segmentation tool (PETTumorSegmentation plugin, 3D Slicer, version 5.2.1) proposed by Beichel et al. (*22*). The SUV$_{\text{mean}}$ was then compared between the motion-corrected and uncorrected average images. The hypothesis was that an increase in SUV should be seen after motion correction because smearing of activity due to motion artifacts is removed.

Robustness and Stability

In addition to the 3 performance measures, we used a fourth measure to characterize the robustness of our algorithm. An ideal diffeomorphic registration algorithm must perfectly align the 2 disparate images and not introduce notable intensity changes during the alignment process. Extreme deformations are observed in the different phases of the contracting heart. We used gated cardiac images to test the robustness and stability of FALCON in preserving image topology and avoiding the introduction of artifacts or intensity changes while handling large deformations. To test the performance of the motion correction, we applied our motion correction algorithm to gated myocardial data obtained using ^{82}Rb PET performed on a Siemens Biograph mCT scanner. This study comprised 11 healthy volunteers who underwent rest myocardial perfusion scans using ^{82}Rb. Each dataset was reconstructed into 8 electrocardiogram phases using an optimized reconstruction window (*23*). All 8 electrocardiogram phases (including the end-systolic phase) were coregistered to the end-diastolic phase. An ideal image-registration algorithm will fully align the end-systolic volume with the end-diastolic volume, yielding stroke volumes and left ventricular ejection fractions of 0 mL and 0, respectively. Although clinically irrelevant, the alignment of all electrocardiogram phases with end-diastole will probe the ability of FALCON to handle large deformations quantitatively. The volumetric analyses were performed in QPET (Cedars-Sinai).

Besides volumetric analyses, left ventricular wall motion is reported for the septum (basal, midventricular, and apical parts) before and after motion correction. In theory, the ideal registration of all phases to the end-diastolic phase would reduce motion to 0 mm for each segment. In contrast, any motion greater than 0 mm reflects residual motion in the image after motion correction. We also report the true motion observed in the heart before motion correction, thus providing insight into how much the motion is constricted when TB motion correction is used. We also investigated the change in intensity introduced by motion correction by generating gated mean images before and after motion correction and compared their line profiles with the reference diastolic phase.

In addition, we quantified the intensity change introduced by the diffeomorphic registration process in noncardiac tracer studies by manually segmenting the brain, kidneys, liver, and spleen in all dynamic frames before and after motion correction. Mean activities (Bq/mL) from all 4 regions were derived for frames before and after motion correction, and the absolute percentage difference was reported.

Statistical Analysis

To test whether applying the motion correction algorithm significantly decreased gross body motion across frames, mismatch volumes derived from the motion-corrected and uncorrected dynamic images were compared using a 2-sample *t* test. Moreover, a 2-sample *t* test was used to determine whether the absolute average distance between the liver dome defined in the reference frame and all other frames differs before and after motion correction. To determine whether SUVs in small tumor nodules increase significantly after motion correction, a paired *t* test was applied between the SUVs before and after motion correction. A *P* value of 0.05 was assumed to indicate statistical significance.

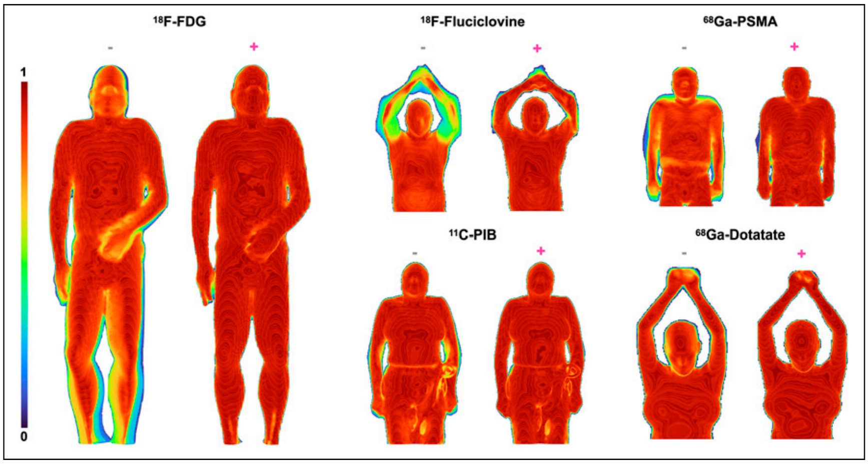

FIGURE 2. Penumbra images generated before (−) and after (+) motion correction for various tracers. Penumbra around extremities is significantly reduced after motion correction.

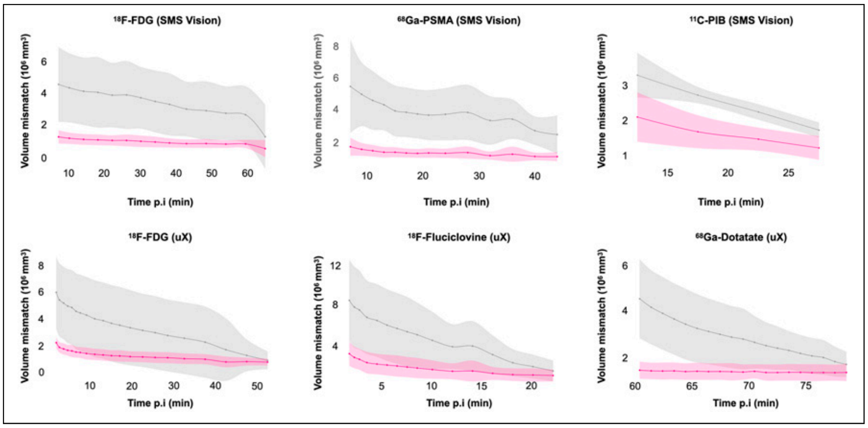

FIGURE 3. Group comparison of average volume mismatch (mm^3) before (gray line) and after (pink line) motion correction across dynamic frames for various tracers and systems. Shaded areas represent 1 SD. After motion correction, both average volume mismatch and associated variance are significantly reduced. p.i = after injection; SMS = Siemens; uX = uEXPLORER.

RESULTS

Selection of Frames for Motion Correction

The candidate frames for motion correction varied depending on the tracer and subject. Therefore, we report the median and interquartile range for each tracer. For dynamic studies using the ^{18}F-FDG and ^{18}F-fluciclovine tracers on the uEXPLORER system, the candidate frames started after 2.5 min (0.7) and 1.8 min (1) after injection, respectively. For ^{68}Ga-DOTATATE scans obtained during the equilibrium phase (60–80 min after injection), the candidate frames started after 2.5 ± 0.7 min and 1.8 ± 1.0 min after injection, respectively. Likewise, for WB imaging studies of ^{18}F-FDG and ^{68}Ga-PSMA involving continuous-bed-motion passes (6–66 min after injection), the candidate frames started 6 min after injection. Finally, for ^{11}C-PIB (10–35 min after injection), the candidate frames began 10 min after injection. Only the candidate frames were subsequently used for motion correction and evaluation purposes.

Correction of Gross Anatomic Motion

Figure 2 shows examples of the penumbra images across the dynamic WB sequence when accounting for gross motion compared with voxel overlap obtained using the uncorrected image volumes. The figure demonstrates improvement in voxel overlap after motion correction, and this improvement can be most clearly appreciated in the decreased shades of the penumbra around the extremities (arms and legs) and the head. Quantitative assessment of gross motion correction showed a substantial reduction in both volume mismatch and the associated variance across the dynamic sequence and various tracers (Fig. 3). On average, volume mismatch decreased by about 50% for ^{18}F-FDG, ^{18}F-fluciclovine, and ^{68}Ga-PSMA image volumes, whereas for ^{11}C-PIB and ^{68}Ga-DOTATATE, it decreased by about 40%. The extended metrics are shown in Table 2.

TABLE 2
Gross Motion Analysis Evaluation for Different Tracer Studies Using Volume Mismatch Metrics

PET/CT system	Tracer	Volume mismatch (%)	*P*
uEXPLORER	^{18}F-FDG	46 ± 14	<0.01
uEXPLORER	^{18}F-fluciclovine	52 ± 9	<0.01
uEXPLORER	^{68}Ga-DOTATATE	43 ± 11	<0.01
Biograph Vision 600	^{18}F-FDG	63 ± 8	<0.01
Biograph Vision 600	^{68}Ga-PSMA	56 ± 10	<0.01
Biograph Vision 600	^{11}C-PIB	36 ± 13	<0.05

Correction of Involuntary Organ Motion

Figure 4 demonstrates virtually perfect alignment of the liver dome across the dynamic sequence in 70% of frames after motion correction. After motion correction, the absolute average distance across the dynamic frames was significantly lower than that determined for the uncorrected images ($P < 0.05$), as seen in Table 3.

Correction of Tumor Tissue Motion

Mean tumor SUVs showed a trend toward an increase in average tracer concentration (15%, $P < 0.01$) between non–motion-corrected images (4.0 ± 2.2) and motion-corrected images (4.6 ± 2.2) (Fig. 5). However, we also observed slight decreases in average tracer concentration in some tumors (presumably tumors without motion) because of the effect of reslicing small volumes.

Assessment of Motion Correction Robustness

Figure 6 shows a representative comparison between the diastolic myocardium and the motion-corrected systolic myocardium from the gated ^{82}Rb images. Our results indicate a substantial decrease (76% ± 3%) in stroke volume after motion correction (from 58 ± 17 mL to 14 ± 4 mL, $P < 0.01$), without leading to anomalous or aberrant distortions in the resulting images. After motion correction, the residual left ventricular wall motion in the basal, mid, and apical anteroseptal regions was reduced by 86%, 81%, and 73%, respectively. In addition, from the intensity profiles of the reference (end-diastolic phase) mean motion-corrected and mean non–motion-corrected images shown in Figure 6, we observe a better overlay of the peaks of the line profile for the mean motion-corrected and reference images than for the mean non–motion-corrected image. The customized analysis clearly indicates preservation of quantitative values.

Likewise, for all noncardiac studies with different tracers, the average absolute percentage difference in intensity in major organs (brain, kidneys, spleen, and liver) was less than 2%, as shown in Supplemental Figures 1–3.

DISCUSSION

We introduce an accurate, fully automated, diffeomorphic motion compensation scheme using both affine alignments and nonrigid deformations of dynamic WB PET images. The algorithm is stable and computationally robust in the presence of substantial organ deformations between image frames, yields subvoxel accuracy in compensating for involuntary body motion over a large range of

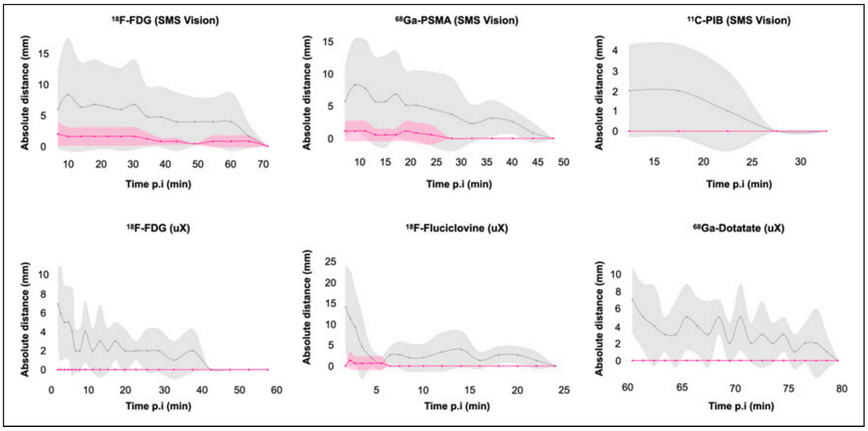

FIGURE 4. Group comparison of absolute difference between reference liver dome (last frame) and remaining dynamic frames for all tracers before (gray line) and after (pink line) motion correction across dynamic frames. Shaded areas represent 1 SD. After motion correction, absolute difference is minimized to zero in most cases. p.i = after injection; SMS = Siemens; uX = uEXPLORER.

PET tracer distribution patterns, and is independent of the acquisition system.

Scale Space Theory for Dynamically Changing Uptake Pattern

Although the time course of distribution is specific for each tracer, the last frame of a dynamic sequence is most commonly selected as the reference frame for alignment of all previous frames. However, accurate alignment of the reference frame with early frames (<10 min after injection) is challenging because of the vastly different uptake patterns and poor count statistics typical of early frames. Therefore, motion correction is typically not performed during the first 10 min (*11*). In our previous work (*4,10*), we used conditional generative adversarial networks to generate PET navigators by converting early frames to frames resembling late frames. The idea was to artificially increase the information in the early frames to resemble the late frames. However, the proposed approach required dedicated hardware (graphics processing unit) and pixelwise spatial correspondence between image pairs, which demanded extensive network training for different tracers—untenable in clinical routine.

Here, we chose a simplified approach that is computationally fast, largely tracer-independent, and does not require any special hardware. First, we identify whether the information in a particular frame is sufficient for alignment based on an objective criterion of uptake pattern similarity. Second, we embed the images in gaussian scale space and conduct the alignment in multiple resolutions. Doing so increases image similarity between early and late frames by suppressing high-frequency information in both frames (*24*). Using this approach, we found that motion could be corrected for frames later than about 2 min after injection for tracers such as ^{18}F-FDG and ^{18}F-fluciclovine.

Motion Correction Assessment

Validation of nonlinear motion correction schemes for organs within the torso is difficult. In radiology, projects such as the Nonrigid Image Registration Project have been established to provide guidelines for validating nonlinear motion correction algorithms for MR and CT images (*25*). Predominantly, these investigators suggest segmenting a specific volume of interest (e.g., liver) in the images to be aligned and quantifying the segmentation overlap before and after alignment. However, this segmentation is not practical in PET imaging, as organ contours in dynamic frames change because of the changing activity distribution and noise over time. Therefore, consensus on a gold standard is needed in the evaluation of nonlinear motion correction algorithms for WB/TB PET motion correction.

In the absence of such a consensus, validation of our method was based on a set of complementing measures that collectively provide a comprehensive assessment of our algorithm's performance. These measures test for the ability to correct for gross body motion, to correct for involuntary movement of a large organ due to respiration within the torso (liver dome), to correct for smearing effects due to motion when small nodules are averaged over multiple frames, and to maintain activity concentration levels even under conditions of substantial deformation.

Clinical Performance

Evaluation of the clinical viability of the method was based on alignment of dynamic image sequences with vastly different uptake

TABLE 3
Organ Motion Evaluation Due to Respiration Before and After Motion Correction for Different Tracer Studies Using Absolute Average Distance Between Liver Dome in Reference Frame and Liver Dome in All Other Frames

		Absolute average distance (mm)		
PET/CT system	Tracer	Before motion correction	After motion correction	*P*
uEXPLORER	^{18}F-FDG	2.7 ± 1.9 (0.0–6.9)	0 (0)	<0.01
uEXPLORER	^{18}F-fluciclovine	4.2 ± 3.9 (0.7–14)	0.3 ± 0.4 (0.0–1.3)	<0.01
uEXPLORER	^{68}Ga-DOTATATE	3.3 ± 1.6 (1.0–7.0)	0 (0)	<0.01
Biograph Vision 600	^{18}F-FDG	5.3 ± 1.7 (1.6–8.4)	1.2 ± 0.5 (0.4–2.0)	<0.01
Biograph Vision 600	^{68}Ga-PSMA	4.8 ± 2.1 (0.9–8.3)	0.6 ± 0.5 (0.0–1.1)	<0.01
Biograph Vision 600	^{11}C-PIB	1.3 ± 1.0 (0.0–2.0)	0 (0)	<0.1

Data in parentheses are range.

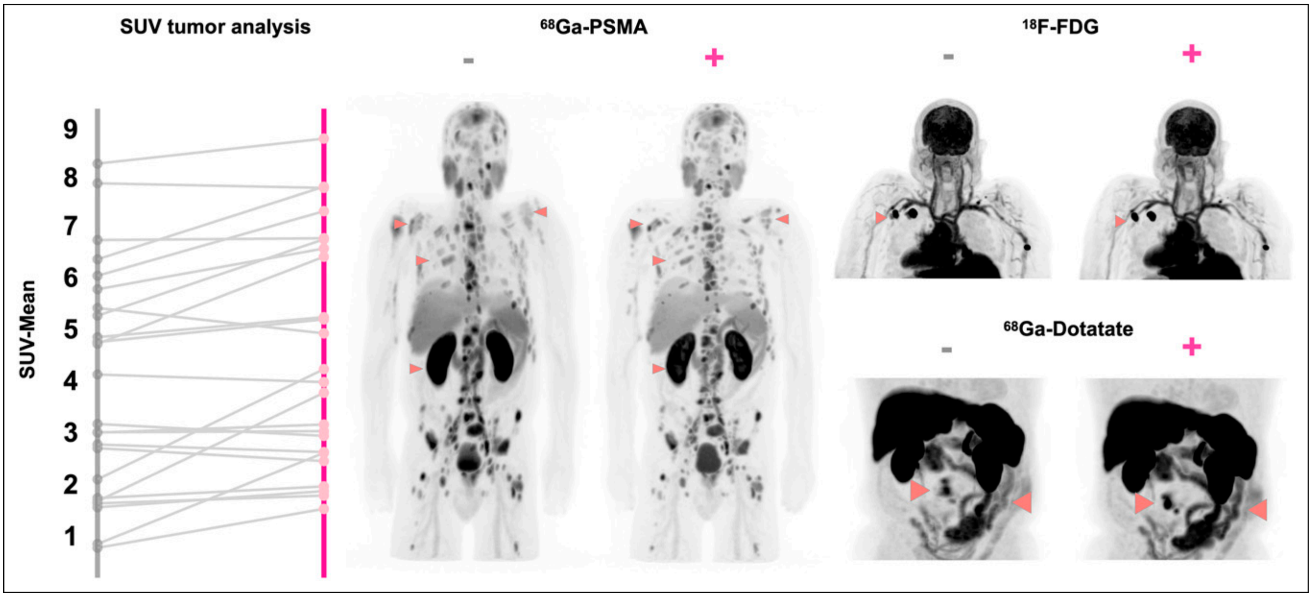

FIGURE 5. Comparison of tumor SUVs from mean images of dynamic series of different tracers before (gray, −) and after (pink, +) motion correction. PET images demonstrate improvement in image quality after correction.

patterns. FALCON proved to serve as a strong baseline motion correction approach that works across different PET/CT systems, tracers, and fields of view. Figures 2 and 3 show the decrease in volume mismatch across the whole body after motion correction. Specifically, one can clearly appreciate the improved diagnostic quality of ^{68}Ga-PSMA images after motion correction (Fig. 5) and a significant decrease in organ movement caused by respiration. This result also suggests the potential of this methodology for correcting motion artifacts in respiration-gated data.

Moreover, one of the major concerns of nonlinear motion correction algorithms is preservation of quantitative aspects of PET data. We investigated these aspects via the intensity profiles of end-diastolic (reference) images, mean motion-corrected images, and mean non–motion-corrected images (Fig. 6) and via multiorgan analysis (Supplemental Figs. 1–3). Our results showed preservation of quantitative values even after large deformations, demonstrated by the improved overlay of line profile peaks in the mean motion-corrected and reference images compared with the mean

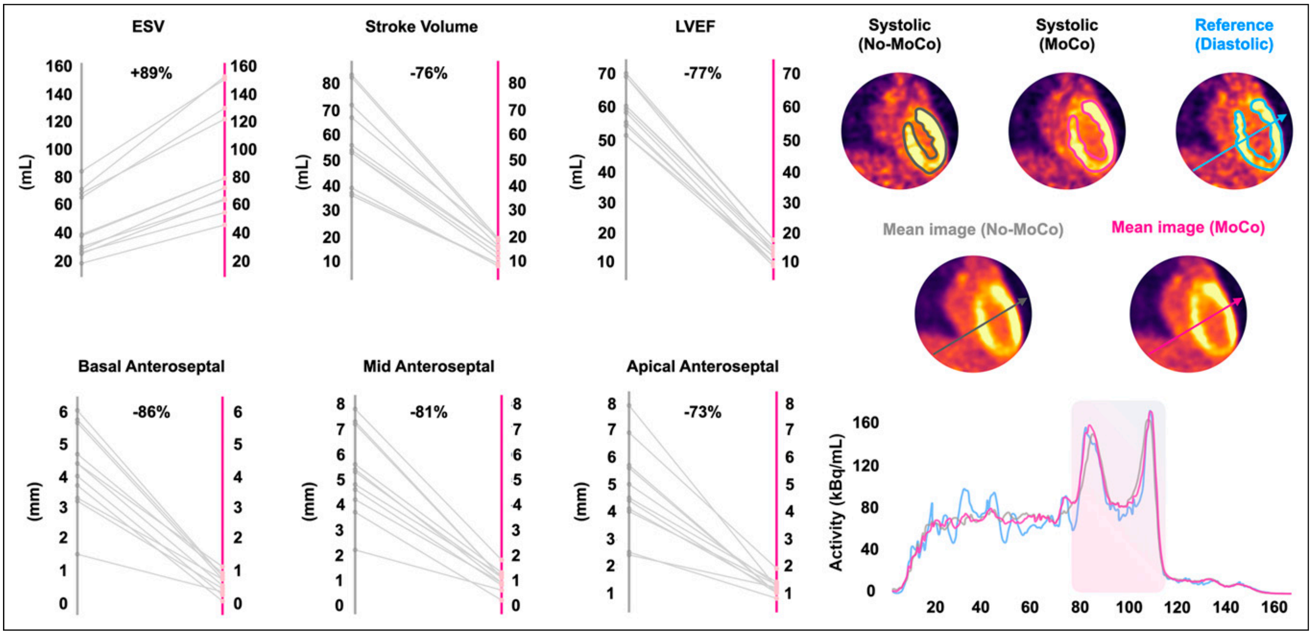

FIGURE 6. Alignment of different gates to end-diastolic phase significantly reduced stroke volume and left ventricular ejection fraction and increased end-systolic volume. Residual motion in basal, mid, and apical regions also was significantly reduced after motion correction. In addition, mean images generated with and without motion correction are shown, with their respective line profiles (motion correction in pink and no motion correction in gray) in comparison to reference diastolic phase (blue). ESV = end-systolic volume; LVEF = left ventricular ejection fraction; MoCo = motion correction.

non–motion-corrected image. In addition, Figure 5 illustrates improved correction of activity smearing, which is clearly visible in the non–motion-corrected images. The average time required for aligning each frame is about 2 min for a TB dataset (typical matrix size, 150 × 150 × 486), with processing time increasing linearly with matrix size. Moreover, using parallel processing on a standard reconstruction server with 32 central-processing-unit cores, FALCON takes about 10 min to correct motion in a dynamic TB dataset consisting of 29 frames.

Limitations

There are several limitations associated with the current implementation. First, we used a static attenuation map that is not motion-corrected; therefore, quantitative errors due to attenuation mismatches are unavoidable (*26,27*). Further, intraframe motion is not addressed in this work. Nonetheless, our results from real-world dynamic studies indicated that even if intraframe motion is not considered, correction of interframe motion can contribute significantly to the quality of summed and parametric images (Supplemental Fig. 4). Finally, FALCON does not allow correction for motion at the beginning of a dynamic sequence (<2 min after injection), when the tracer distribution pattern differs substantially from the reference image. Using FALCON to correct for frames during the first pass will provide poor results. Our validation studies suggest that the tracer distribution patterns in image frames acquired during the initial 120 s are significantly different from the pattern in the reference image (even at the lowest-resolution scale), precluding successful application of our method in these very early frames. Although these frames are generally less important from a clinical point of view, they carry information about the blood input function, which is often of interest to obtain an image-derived input function for kinetic modeling (*28*) and quantification (*29*). Consequently, motion correction of these early frames will require a separate alignment strategy.

Finally, because of filling of the bladder, FALCON tends to warp the semifilled bladder of the moving frames to the filled bladder of the reference frame. Therefore, care should be taken in interpreting the bladder area after motion correction. Likewise, we have observed that FALCON performs poorly in correcting large-angle joint flexions and extensions, such as large finger motions.

CONCLUSION

The developed motion correction tool, FALCON, allows correction of rigid and nonlinear motion that might be present in WB dynamic imaging studies. Our software tool can potentially improve the accuracy of PET scans, ultimately leading to better diagnosis and treatment.

DISCLOSURE

This work was partly supported by NIH research grant R01CA29422 and by ERA-PERMED 2021-324 PETictCAC. No other potential conflict of interest relevant to this article was reported.

KEY POINTS

QUESTION: Is there a clinically viable method of correcting motion in WB dynamic PET imaging data?

PERTINENT FINDINGS: FALCON, a fast, fully automated WB motion correction tool that is independent of vendor, tracer distribution, and axial field of view, is proposed. FALCON is based on Greedy diffeomorphic registration paradigms and shows promise in improving voxel overlap, reducing gross volume mismatch, and increasing tumor contrast. FALCON is computationally stable and robust, permitting correction of even large deformations associated with the beating heart without leading to topologic or intensity aberrations.

IMPLICATIONS FOR PATIENT CARE: FALCON allows accurate and consistent correction of motion artifacts in WB PET scans regardless of the external markers, tracer, or scanner geometry. Consequently, FALCON might contribute to improved performance in the clinical setting.

REFERENCES

1. Badawi RD, Shi H, Hu P, et al. First human imaging studies with the EXPLORER total-body PET scanner. *J Nucl Med.* 2019;60:299–303.
2. Zhang X, Cherry SR, Xie Z, Shi H, Badawi RD, Qi J. Subsecond total-body imaging using ultrasensitive positron emission tomography. *Proc Natl Acad Sci USA.* 2020;117:2265–2267.
3. Lu Y, Naganawa M, Toyonaga T, et al. Data-driven motion detection and event-by-event correction for brain PET: comparison with Vicra. *J Nucl Med.* 2020;61:1397–1403.
4. Shiyam Sundar LK, Iommi D, Muzik O, et al. Conditional generative adversarial networks aided motion correction of dynamic ^{18}F-FDG PET brain studies. *J Nucl Med.* 2021;62:871–879.
5. Spangler-Bickell MG, Khalighi MM, Hoo C, et al. Rigid motion correction for brain PET/MR imaging using optical tracking. *IEEE Trans Radiat Plasma Med Sci.* 2019;3:498–503.
6. Rubeaux M, Doris MK, Alessio A, Slomka PJ. Enhancing cardiac PET by motion correction techniques. *Curr Cardiol Rep.* 2017;19:14.
7. Lassen ML, Tzolos E, Pan T, et al. Anatomical validation of automatic respiratory motion correction for coronary ^{18}F-sodium fluoride positron emission tomography by expert measurements from four-dimensional computed tomography. *Med Phys.* 2022;49:7085–7094.
8. Nehmeh SA. Respiratory motion correction strategies in thoracic PET-CT imaging. *PET Clin.* 2013;8:29–36.
9. Kesner AL, Schleyer PJ, Büther F, Walter MA, Schäfers KP, Koo PJ. On transcending the impasse of respiratory motion correction applications in routine clinical imaging: a consideration of a fully automated data driven motion control framework. *EJNMMI Phys.* 2014;1:8.
10. Sundar LS, Iommi D, Spencer B, et al. Data-driven motion compensation using cGAN for total-body [^{18}F]FDG-PET imaging [abstract]. *J Nucl Med.* 2021;62(suppl 1):35.
11. Sun T, Wu Y, Wei W, et al. Motion correction and its impact on quantification in dynamic total-body ^{18}F-fluorodeoxyglucose PET. *EJNMMI Phys.* 2022;9:62.
12. Venet L, Pati S, Feldman MD, Nasrallah MP, Yushkevich P, Bakas S. Accurate and robust alignment of differently stained histologic images based on Greedy diffeomorphic registration. *Appl Sci (Basel).* 2021;11:1892.
13. Miller MI, Joshi SC, Christensen GE. Large deformation fluid diffeomorphisms for landmark and image matching. In: *Brain Warping.* Elsevier; 1999:115–131.
14. Vercauteren T, Pennec X, Perchant A, Ayache N. Symmetric log-domain diffeomorphic registration: a demons-based approach. *Med Image Comput Comput Assist Interv.* 2008;11:754–761.

15. Ashburner J. A fast diffeomorphic image registration algorithm. *Neuroimage.* 2007;38:95–113.
16. Avants BB, Epstein CL, Grossman M, Gee JC. Symmetric diffeomorphic image registration with cross-correlation: evaluating automated labeling of elderly and neurodegenerative brain. *Med Image Anal.* 2008;12:26–41.
17. Santos J, Chaudhari AJ, Joshi AA, et al. Non-rigid registration of serial dedicated breast CT, longitudinal dedicated breast CT and PET/CT images using the diffeomorphic demons method. *Phys Med.* 2014;30:713–717.
18. Cormen TH, Leiserson CE, Rivest RL, Stein C. *Introduction to Algorithms.* 4th ed. MIT Press; 2001.
19. Thevenaz P, Ruttimann UE, Unser M. Iterative multi-scale registration without landmarks. In: *Proceedings, International Conference on Image Processing.* Vol 3. IEEE; 1995:228–231.
20. McCormick M, Liu X, Jomier J, Marion C, Ibanez L. ITK: enabling reproducible research and open science. *Front Neuroinform.* 2014;8:13.
21. Yoo TS, Ackerman MJ, Lorensen WE, et al. Engineering and algorithm design for an image processing Api: a technical report on ITK—the Insight Toolkit. *Stud Health Technol Inform.* 2002;85:586–592.
22. Beichel RR, Van Tol M, Ulrich EJ, et al. Semiautomated segmentation of head and neck cancers in ^{18}F-FDG PET scans: a just-enough-interaction approach. *Med Phys.* 2016;43:2948–2964.
23. Lassen ML, Wissenberg M, Byrne C, Kjaer A, Hasbak P. Optimization of the left ventricle ejection fraction estimate obtained during cardiac adenosine stress ^{82}rubidium-PET scanning: impact of different reconstruction protocols. *J Nucl Cardiol.* 2022;29:3369–3378.
24. Gutschmayer S, Muzik O, Chalampalakis Z, et al. A scale space theory based motion correction approach for dynamic PET brain imaging studies. *Front Phys.* 2022;10:1034783.
25. Christensen GE, Geng X, Kuhl JG, et al. Introduction to the non-rigid image registration evaluation project (NIREP). In: *Biomedical Image Registration: Lecture Notes in Computer Science.* Springer; 2006:128–135.
26. Le Meunier L, Maass-Moreno R, Carrasquillo JA, Dieckmann W, Bacharach SL. PET/CT imaging: effect of respiratory motion on apparent myocardial uptake. *J Nucl Cardiol.* 2006;13:821–830.
27. Emond EC, Bousse A, Machado M, et al. Effect of attenuation mismatches in time of flight PET reconstruction. *Phys Med Biol.* 2020;65:085009.
28. Shiyam Sundar LK, Muzik O, Rischka L, et al. Promise of fully integrated PET/MRI: noninvasive clinical quantification of cerebral glucose metabolism. *J Nucl Med.* 2020;61:276–284.
29. Wang G, Nardo L, Parikh M, et al. Total-body PET multiparametric imaging of cancer using a voxelwise strategy of compartmental modeling. *J Nucl Med.* 2022; 63:1274–1281.